Published in final edited form as:
Nature. 2017 July 20; 547(7663): 350–354. doi:10.1038/nature23015.

Cholangiocytes act as Facultative Liver Stem Cells during Impaired Hepatocyte Regeneration

Alexander Raven[#1], **Wei-Yu Lu**[#1], **Tak Yung Man**[1], **Sofia Ferreira-Gonzalez**[1], **Eoghan O'Duibhir**[1], **Benjamin J Dwyer**[1], **John P Thomson**[2], **Richard R Meehan**[2], **Roman Bogorad**[3], **Victor Koteliansky**[4], **Yuri Kotelevtsev**[4], **Charles ffrench-Constant**[1], **Luke Boulter**[2], and **Stuart J Forbes**[1]

[1]MRC Centre for Regenerative Medicine, University of Edinburgh, 5 Little France Drive, Edinburgh, EH16 4UU, UK

[2]MRC Human Genetics Unit, Institute of Genetics and Molecular Medicine, Edinburgh EH4 2XU, UK

[3]David H. Koch Institute for Integrative Cancer Research, Massachusetts Institute of Technology, Cambridge, MA 02139, USA

[4]Functional genomics and RNAi therapy CREI, Skolkovo Institute for Science and Technology, 3 Nobel street, Skolkovo Moscow region, 143026, Russian Federation

[#] These authors contributed equally to this work.

Summary

Following liver injury, regeneration occurs through self-replication of hepatocytes. In severe liver injury, hepatocyte proliferation is impaired, a feature of human chronic liver disease1,2. It is contested whether other liver cell types can regenerate hepatocytes3–5. Here, we use two independent systems to impair hepatocyte proliferation during liver injury to evaluate the contribution of non-hepatocytes to parenchymal regeneration. Firstly, loss of β1-Integrin in hepatocytes with liver injury triggered a ductular reaction of cholangiocyte origin, and ~25% of hepatocytes being derived from a non-hepatocyte origin. Secondly cholangiocytes were lineage traced with concurrent inhibition of hepatocyte proliferation by β1-Integrin knockdown or p21

Contact: Stuart J Forbes, MRC Centre for Regenerative Medicine, University of Edinburgh, 5 Little France Drive, Edinburgh, EH16 4UU. stuart.forbes@ed.ac.uk.

Author Contributions

A.R.: performed the β1-Integrin experiments, experimental design, data generation, data analysis and interpretation, manuscript preparation W.Y.L.: performed the AAV8-p21 experiments, experimental design, data generation, data analysis and interpretation, manuscript preparation S.G.: performed partial hepatectomy, critiqued manuscript T.Y.M.: performed immunostaining E.O.D.: data analysis, B.D.: critiqued manuscript, performed western blot J.P.T, R,R.M.: performed the RNA sequencing and analysis R.B, V.K, Y.K.: provided the nanoparticles C.F.C.: critiqued manuscript L.B.: experimental and study design, critiqued manuscript S.J.F.: conception and study design, data interpretation, manuscript preparation.

Competing financial interests

The authors declare no competing financial interests.

Data availability

Data generated during this study are available in the Gene Expression Omnibus (GEO) repository under accession number GSE98034. All other data are available from the corresponding author upon reasonable request.

Europe PMC Funders Author Manuscripts

over-expression, resulting in the significant emergence of cholangiocyte derived hepatocytes. We describe a model of combined liver injury and inhibition of hepatocyte proliferation that causes physiologically significant levels of regeneration of functional hepatocytes from biliary cells.

The identification of a liver stem or progenitor cell remains elusive6. Transplanted biliary progenitors can partly repopulate the liver's hepatocyte population7,8 but it is still unproven whether endogenous biliary cells can regenerate hepatocytes3,4. Severe liver injury in human and animals impairs hepatocyte proliferation and causes ductular reactions (DR) to emerge2,9,10. DRs may arise from the biliary epithelium11,12 or via de-differentiation of hepatocytes13. Biliary cells in zebrafish models have been shown to regenerate the liver after massive hepatocytes loss9, however, this remains unproven in mammalian systems3,4,14. Lineage tracing of biliary DRs into new hepatocytes, in the mouse, is dependent on both the severity and type of liver injury model, which have shown an inconsistent and limited contribution to hepatocyte regeneration3,4,15,16. Murine lineage tracing experiments, do not typically recapitulate human disease, as significant hepatocyte replication is seen alongside DRs. We therefore sought to develop a model in which DRs occur on the background of impaired hepatocellular regeneration and evaluate the regenerative capacity of the DRs.

We lineage traced hepatocytes using the highly efficient viral AAV8.TBG.Cre injected into a $R26R^{LSL}$tdTomato mouse, thereby activating tdTomato (tdTom) expression in over 99.5% of hepatocytes (Extended Data Fig. 1a,b). These mice had either wild type *Itgb1* (β1-$Integrin^{WT}$), or mutated *Itgb1* (β1-$Integrin^{fl/fl}$) (Extended Data Fig. 1c-e), previously shown to eliminate β1-Integrin expression17, thereby inhibiting hepatocyte growth factor signalling and impairing regeneration18.

AAV8.TBG.Cre mediated β1-Integrin ablation caused parenchymal damage with raised serum markers and cytoplasmic localisation of High Mobility Group Box 1 protein (HMGB1), a DAMP associated with liver necrosis and inflammation 19 (Extended Data Fig. 2a,b, arrows). There was a prominent DR in β1-$Integrin^{fl/fl}$ livers compared to control β1-$Integrin^{WT}$ livers, with increased biliary cytokeratin 19 positive ($CK19^{pos}$) cells and alpha smooth muscle actin positive (αSMA^{pos}) myofibroblasts. $CK19^{pos}$ cells were distributed throughout the parenchyma (Extended Data Fig. 2c,d,e). β1-$Integrin^{fl/fl}$ livers had small areas of tdTom negative ($tdTom^{neg}$) hepatocytes adjacent to the portal tracts (Extended Data Fig. 2c,f). Furthermore, β1-$Integrin^{fl/fl}$ livers contained more Ki67 positive hepatocytes (proliferating marker) and more $p21^{pos}$ hepatocytes (cell cycle arrest marker) (Extended Data Fig. 2g,h).

We damaged β1-$Integrin^{WT}$ and β1-$Integrin^{fl/fl}$ livers with 3 independent regimes; DDC diet, a model of cholestatic liver disease; Methionine and Choline Deficient (MCD) diet, a model of non-alcoholic steatohepatitis and thioacetamide (TAA), a model of liver fibrosis20 and studied the regenerative dynamics (Fig. 1a). After DDC injury, all mice lose weight but β1-$Integrin^{fl/fl}$ mice had delayed weight recovery. β1-$Integrin^{fl/fl}$ mice had prolonged hepatocellular Ki67 and p21 expression; and elevated serum markers of liver injury (Extended Data Fig. 3a-d) indicating that following β1-Integrin loss hepatocytes are unable to regenerate the injured liver efficiently. Hepatocyte Ki67 and p21 expression was rarely co-

localised (Extended Data Fig. 3e). β1-Integrin$^{fl/fl}$ livers had increased liver necrosis and recovered slowly from DDC injury (Extended Data Fig. 3f,g, asterisks). There were increased DRs following hepatocyte β1-Integrin loss, demonstrating that the DDC induced injury remains unresolved in the absence of hepatocyte β1-Integrin (Fig. 1b). Persistent DRs were also found in β1-Integrin$^{fl/fl}$ livers that were injured with MCD and TAA (Fig. 1c). Following hepatocyte β1-Integrin loss DDC induced DRs had atypical biliary cells, not confined to luminal structures (Fig. 1e, arrowheads and Extended Data Fig.4a, arrows). DRs in β1-Integrin$^{fl/fl}$ livers were surrounded by αSMA^{pos}, myofibroblasts that peaked in number by day 7 recovery, however, the degree of fibrosis increased throughout recovery (Fig. 1d,e and Extended Data Fig. 3h,i).

To determine if non-hepatocytes regenerated hepatocytes we examined tdTom expression. Following liver injury and recovery with DDC, MCD and TAA, 20-30% of CYP2D and HNF4α (mature hepatocyte markers) positive hepatocytes were tdTom^{neg} (Fig. 1f-h and Extended data Fig. 4a,b). Small, proliferative tdTom^{neg} hepatocytes were identified from day 7 and increased significantly until day 14 (Extended data Fig. 4c-e). tdTom^{neg} hepatocytes were normally found adjacent to SOX9^{pos} and CK19^{pos} ductal cells, and the number of tdTom^{neg} hepatocytes decreased with distance from DRs (Fig. 2a,b). SOX9^{pos}/tdTom^{neg}/HNF4α^{pos} cells could be seen at the border between unlabelled parenchyma and DRs (Fig. 2a), and putatively represent an intermediate cell state between ductular cells and hepatocytes. At day 14 of recovery tdTom^{neg} hepatocyte patches had formed nodules; remaining tdTom^{pos} hepatocytes were arranged around glutamine synthetase (GS) positive central vein hepatocytes (Extended data Fig. 4f,g). The distribution of tdTom^{neg} hepatocytes suggested a ductular origin, we therefore genetically labelled biliary cells and concurrently supressed *Itgβ1* expression specifically in hepatocytes with lipid coated RNAi nanoparticles18,21 (Fig. 2c). The *CK19*^{CreERT}*tdTomato*^{LSL} lineage-tracing model specifically labels the biliary epithelium with a 40% recombination efficiency, and stringently excludes the hepatocyte lineage (Extended data Fig. 5a,b). Following β1-Integrin RNAi treatment and DDC or MCD injury, cholangiocyte derived periportal E-cadherin^{pos}/tdTom^{pos}/HNF4α hepatocytes were detected compared to RNAi controls (Fig.2d).

In humans, increased expression of p21 in hepatocytes is seen in chronic liver disease, suggesting that hepatocyte replicative potential becomes exhausted1,2. We sought to reproduce this in our mouse models of liver injury and regeneration by impairing hepatocyte proliferation to mobilize a traceable, biliary-derived hepatocyte regenerative response. To achieve this we utilized a p21 coding region inserted into an AAV8 vector downstream of a Thyroxine Binding Globulin (TBG) promoter22 to overexpress p21 in hepatocytes (Fig 3a). Liver *Cdkn1a* mRNA expression was 6 times higher in the AAV8-p21 injected group (Fig 3b) Hepatocyte p21 expression was observed after injection of the AAV8-p21 (Fig 3c). Liver histology remained normal (Extended Data Fig. 6a,b). Proliferating non-parenchymal cells were seen close to the portal tracts (Fig 3d). Additionally, no significant changes in DR or collagen deposition were detected following p21 over expression (Extended Data Fig. 6c,d). To confirm that p21 overexpression was sufficient to inhibit hepatocyte proliferation, we induced acute liver injury post AAV8 injection (Fig. 3e). Ki67^{pos}/HNF4α^{pos} hepatocytes were only present in mice that received the AAV8-ctrl vector (Fig. 3f), and p21 expression was increased in the AAV8-p21 group (Fig 3f,g). No significant changes in necrotic area

was observed (Fig 3h), although serum transaminases were higher in the AAV8-p21 group (Fig 3i).

To induce DRs on the background of impaired hepatocyte proliferation we used the Choline Deficient Ethionine supplemented (CDE) Diet combined with AAV8-p21 or AAV8-ctrl (Extended Data Fig. 7a). Hepatocyte proliferation was inhibited in mice in the AAV8-p21 group (Extended Data Fig. 7b,d). Proliferating cells observed in the AAV8-p21 injected group were HNF4α^{neg} (Extended Data Fig. 7c). After CDE injury, there was a trend to increased DRs in the AAV8-p21 group (Extended Data Fig. 7e). The AAV8-p21 group had persistent hepatocellular p21 expression 2 weeks after injury compared to control (Extended Data Fig. 7f). mRNA analysis showed a 5-fold increase in *p21* expression and liver damage related genes such as *Igfbp1* and *Tgfb1* increased 20-fold and 2-fold respectively. In addition, a 4-fold increase in the DR gene *Krt19* was found (Extended Data Fig. 7g). Together, these findings demonstrate that AAV8-p21 administration causes hepatocyte p21 accumulation and impaired hepatocyte proliferation following injury.

We used the *CK19*^{CreERT}*tdTomato*^{LSL} lineage-tracing model to test whether cholangiocytes gave rise to hepatocytes in various diet induced liver injuries combined with p21 over expression (Fig 4a). After the CDE, MCD, or DDC injury regimes (Fig.4a, Extended Data Fig. 8a,f), tdTom expressing hepatocytes were observed in the AAV8-p21 group (Fig4b, Extended Data Fig. 8 b,c,g,h). tdTom^{pos} cells contributed to 6.12 ± 0.3% of the liver 2 weeks after injury (Fig.4b). Considering that the *Krt19*^{CreERT}*tdTomato*^{LSL} system labels approximately 40% of all biliary cells we corrected for this limitation in recombination efficiency, predicting that biliary cells differentiate into approximately 15.3 % of hepatocytes in this model. Periodic acid–Schiff staining of serial liver sections show the tdTom^{pos} hepatocytes store glycogen (Fig 4c). Other hepatocyte markers such as HNF4α, GS, and CYP2D were expressed by these cholangiocyte derived tdTom^{pos} hepatocytes (Fig 4d, Extended Data Fig 8d,i and 9a). These cholangiocyte derived hepatocytes were present 10 weeks after injury (Extended Data Fig 9 b,c,d,e). Periportal tdTom^{pos}, SOX9^{neg} hepatocytes were adjacent to the tdTom^{pos}, SOX9^{pos} DRs suggesting differentiation of SOX9^{pos} ductular cells into hepatocytes (Fig. 4e, Extended Data Fig 8e). tdTom^{pos} hepatocytes expressing HNF4α and zone 1 marker E-Cadherin were directly adjacent to the tdTom^{pos} and PanCK^{pos} cholangiocytes in keeping with their ductular origin (Fig. 4f). To test the proliferative capacity of the cholangiocyte derived tdTom^{pos} hepatocytes, we performed 50% partial hepatectomy following MCD injury/recovery (Extended Data Fig. 9f). Fewer hepatocytes in AAV8-p21 group were proliferative following hepatectomy (Extended Data Fig 9g) and periportal tdTom^{pos} Ki67^{pos} E-Cadherin^{pos} proliferating hepatocytes were observed in the AAV8-p21 group (white arrows) (Extended Data Fig. 9h). These results confirm the direct contribution of labelled cholangiocytes to hepatocyte regeneration during injury when hepatocyte proliferation is inhibited. To compare hepatocytes of different origins, we isolated: non-hepatocyte derived hepatocytes from the β1-Integrin$^{fl/fl}$ model (tdTom^{neg}), cholangiocyte derived hepatocytes from the AAV8-p21 model (tdTom^{pos}) (Extended data Fig.10a-c) and compared against hepatocytes and cholangiocytes from injured wild-type mice. Gene expression between these cells was assessed with a drug metabolism qPCR array and RNAseq. Global transcriptional states of the biliary derived hepatocytes from AAV8-p21 treated livers and tdTom^{neg} hepatocytes from the β1-Integrin$^{fl/fl}$ model were highly

similar to hepatocytes and distinct from ductal cells (Fig. 4g, Extended Data Fig. 10d,e,f). $tdTom^{pos}$ hepatocytes clustered closely with control wild-type hepatocytes (Fig. 4h). Differences in the newly formed $tdTom^{neg}$ hepatocytes from the β1-$Integrin^{fl/fl}$ model may be explained by the continued presence of defective β1-$Integrin^{fl/fl}$ hepatocytes in the liver and their effect upon the tissue microenvironment (Extended Data Fig. 10e,f).

Impaired hepatocyte regeneration has been studied in two independent systems; hepatocyte β1-Integrin ablation, and p21 over-expression. Both models triggered DRs followed by clusters of cholangiocyte derived hepatocytes. Multiple hepatocyte sub-populations have been suggested as regenerative under homeostasis23,24 or liver injury14. However, our findings show that whilst DRs can be generated following injury, impaired hepatocyte regeneration is required for cholangiocytes to form hepatocytes. The mechanism of effect of the two models is different: β1-Integrin ablation causes hepatocyte necrosis, p21 expression and inhibition of growth factor signalling,18 and viral p21 overexpression directly inhibits hepatocyte proliferation; the common factor being impaired hepatocyte regeneration. This explains previous conflicting data from mouse, rat and human disease, where the lack of differentiation seen in lineage tracing models is likely due to ongoing effective hepatocyte mediated regeneration. The full potential of cholangiocyte derived hepatocyte regeneration may be higher as these are short term injury models compared to human liver disease. These systems have now identified the cellular sources of regeneration in severely injured adult liver. This will facilitate studies into the signals controlling this regenerative pathway, aiding the development of liver regeneration therapies.

Methods

Animal models

The animals in this study were on a C57BL6/J background. Both male and female mice were used. Animals were housed in a specific pathogen-free environment and kept under standard conditions with a 12 hour day/night cycle and access to food and water ad libitum. All animal experiments were carried out under procedural guidelines, severity protocols and with ethical permission from the University of Edinburgh Animal Welfare and Ethical Review Body (AWERB) and the Home Office (UK).

To delete β1-Integrin *in vivo,* we utilised the β1-$Integrin^{fl/fl}$ mice (The Jackson Laboratory), this model has exon 3 of β1-Integrin gene is flanked by loxP sites 17. To lineage trace β1-$Integrin^{fl/fl}$ cells we crossed this strain with the $R26RtdTomato^{LSL}$ mouse (The Jackson Laboratory).

Genotyping was performed by the Transnetyx genotyping service.

Mice between 7-10 weeks of age had Cre mediated recombination induced with AAV8.TBG.Pi.Cre.rBG (Penn vector core, CS0644). Control, null, experiments used AAV8.TBG.Pi.null.rBG (Penn vector core, CS0255).Viruses were administrated by tail vein injection at a concentration of $2.5X10^{11}$ GC/ml. AAV8 viruses were diluted in sterile PBS. Mice were given a 2 week wash out period before being placed on toxic injury diets.

Small interfering RNA (siRNA) formulated in to lipidoid nanoparticles were used to silence Itgβ1 mRNA *in vivo*. These siRNA nanoparticles have been previously shown to specifically suppress hepatocyte β1 integrin expression18,21. 0.5mg/kg doses were administrated intravenously via the tail vein to each mouse every 5 days according to the schematic in Fig. 2e.

The $Krt19^{Cre}TdTomato^{LSL}$ mice was induced by 3 individual i.p. injections of Tamoxifen (20mg/ml, Sigma UK) at the dose of 4mg. K19Cre animals received two weeks of normal diet after the last Tamoxifen injection before commencing an injury diet regime.

To induce liver injury mice were given 0.1% 3,5-Diethoxycarbonyl-1,4-dihydrocollidine (DDC) mixed with Rat & Mouse No1 Maintenance (RM1) diet (Special Diet Services), for 7-10 days; the Methionine and Choline Deficient (MCD) diet (MP Biomedicals) was given for 7-14 days; Thioacetamide (TAA) (Sigma Aldrich) was administered in the drinking water at a concentration 300mg/L for 21 days; the choline deficient ethionine supplemented (CDE) diet began with a choline sufficient CDE weaning diet for 1 week (MP Biomedicals, 960412) followed by 3 weeks of CDE diet (custom made by MP biomedicals). After injury diet mice were given normal chow and drinking water. For the CCL_4 injury model mice received one IP injection of CCL4 at a dose of 1ml/Kg and were then euthanized 48 hours later.

50% Partial Hepatectomy was carried out under isoflurane anaesthesia, median laparotomy was performed followed by removal of the left lateral and upper left median lobe, as previously described25. Mice were sacrificed at 48 hours after surgery.

Mice were euthanized according to UK Home Office regulations. Blood was collected by cardiac puncture and centrifuged to collect serum. Organs were harvested and either directly frozen at -80°C or fixed in 10% formalin (in PBS) for 12 hours. Formalin fixed tissue was then stored in paraffin. Animals due to reaching experimental severity protocol boundaries were excluded from analysis. Otherwise all animals were included in analysis. Animal studies are used throughout in this work. Power calculations were not routinely performed; however animal numbers were chosen to reflect the expected magnitude of response taking into account the variability observed in previous experiments.

AAV8-p21 design and *in vivo* delivery

pGEM p21 was a gift from Dr Frederic Mushinski (Addgene plasmid # 8443). The p21 plasmid was packaged into the AAV8.TBG vector by Penn Vector Core. AAV8-Ctrl plasmid (AAV8.TBG.PI.Null.bGH, Cat No: AV-8-PV0148) was obtained from Penn Vector Core. 7.5×10^{11} viral particles were reconstituted in 100μL injected intravenously through tail vein injection with BD Ultra-Fine Insulin Syringes.

Histology, immunohistochemistry and immunofluorescence

Formalin fixed tissue embedded in paraffin. 4μm sections were blocked with protein block (Spring Bioscience) and stained overnight at 4°C using antibodies listed in supplementary table 1. Primary antibodies were detected using fluorescent conjugated secondary antibodies (alexa 488/alexa555 and alexa657; invitrogen). Sections were stained with Dapi and

mounted with fluromount (SouthernBiotech). For DAB stained sections tissue was blocked with Bloxall (Vector), Avidin/Biotin block (Invitrogen) and protein block. Primary antibodies were incubated overnight at 4°C. Species specific secondary biotinylated antibodies (Vector), Vectastain R.T.U, ABC reageant (Vectar) and DAB chromogen (Dako) were used to detect the primary antibody. Haematoxylin counter stain was used alongside the DAB.

When two antibodies from the same species were used, Sox9/RFP/HNF4α immunofluorescent stain, primary antibodies were applied sequentially. The first antibody to be applied, anti-RFP, was detected using a species specific secondary antibody (Dako) conjugated to HRP and a Perkin Elmer TSA Plus Cyanine 3, signalling amplification, kit (NEL744B001KT). This was followed by a second antigen retrieval to denature any antibodies in the tissue and prevent cross-reaction with the following antibody application.

Heamatoxylin and Eosin (H&E) stains were automatically produced using a Shandon Varistain Automated Slide Stainer. PicroSirius Red (PSR) stains used reagents from Sigma Aldrich; picric acid Cat No:P6744-1GA, fast green Cat No:F7258-25G, direct red Cat No: 365548-25G. Staining was done according to manufacturer's instructions.

Microscopy and cell counting

For confocal microscopy either a Leica SPE inverted microscope or a Zeiss LSM 780 confocal microscope were used and images were deconvoluted using Fiji ImageJ. Brightfield images were taken using a Nikon Eclipse e600 microscope and Retiga 2000R camera (Q-Imaging) and acquired with image pro premier software. PSR anaylsis used an AxioScan Z. 1 (Zeiss) to acquire tiled images at a 20X magnification. De-tiled images were then analysed using a standard colour threshold in Fiji Image J. Necrotic areas were quantified using haematoxylin and eosin (H&E) histochemistry and the trainable WEKA segmentation tool in Fiji Image J.

Fluorescent tiled images were generated on a Perkin Elmer Operetta high content imaging system, subsequent image stitching was done on Fiji ImageJ using the pairwise stitching plugin 26. DAPI, Alexafluor 488, and 555 were detected using band paths of 415-480, 495-540 and 561-682nm for 405, 488 543 nm lasers respectively.

In cases which manual quantification was performed (including animal experiments), counts were performed manually on blinded slides and more than 20 consecutive non overlapping fields at x100 or x200 magnification.

Single Cell Liver tissue analysis

Images were acquired in up to four fluorescent channels at 10X magnification on a Perkin Elmer Operetta high content imaging system and subsequently analysed using the Columbus software. An average of 25 images were taken per liver section. One field of view corresponds to 1.37mm2. Dapi stained nuclei were identified based on pixel intensity using method 'M' with approximately 7000 nuclei identified per field. Nuclear size and morphology was then determined. Illumination correction and background normalization was performed using the sliding parabola module. Depending on the experiment nuclei were

then assigned as positive or negative based on the mean pixel intensity in the corresponding channel in either the nucleus (HNF4α, tdTomato, Ki67, P21 and PCNA) or a 7μm thick region surrounding the nucleus (CK19 and αSMA). For each experiment identical thresholds were used in all images for assigning nuclei to a specific population.

Protein homogenates and western blots

Protein was isolated from whole liver. Small, 1-2mm2 pieces of liver were homogenised using a tissue tearor (Biospec Products) and lysis buffer (lysis buffer: 150mM NaCl, 20mM Tris pH7.5, 1mM EGTA, 1mM EDTA, 1% Triton X-100, 2X Protease inhibitor Cocktail(Sigma Aldrich)). Samples were mixed at 4°C for 30 minutes and then centrifuged for 10 minutes at 20'000g. The aqueous supernatant was removed and the protein concentration was determined using a Pierce BCA Protein Assay Kit (Thermo Scientific). Proteins were separated using SDS-page and transferred to nitro cellulose membranes, anti-β1-Integrin (Millipore, MAB1997) 1/1000 and anti-β-actin (Cambridge Biosciences) 1/2000 were used to detect proteins.

Isolation of Biliary Ducts, Hepatocytes and Fluorescence Activated Cell Sorting (FACS)

Hepatocytes and biliary ducts were isolated using the classical perfusion protocol. Briefly, animals received an overdose of anaesthetic followed by laparotomy, the portal vein was cannulated and injected with Liver Perfusion Medium (Gibco) and Liver Digest Medium (Gibco). For ducts isolation, ducts were digested and isolated as previously described8. For hepatocyte isolation, the liver was removed and mechanically disaggregated. The resulting disassociated cells were filtered through a 70μm filter (BD Biosciences). Hepatocytes were purified with a density gradient centrifugation27, which isolates cells with hepatocyte morphology and expression of CYP2D6 (a mature hepatocyte marker) at a purity over 99%7. Briefly, cells were layered above various Percoll solutions, 1.06, 1.08 and 1.12 g/ml Percoll (Sigma) in PBS. Cells were spun at 750xG 20 min. The hepatocyte layer, between the 1.08 and 1.12 mg/ml Percoll layers, was collected for FACS. Purified Hepatocytes were sorted on a BD biosciences Fusion Flow Cytometer. Sorted cells where lysed and the RNA was extracted.

RNA isolation and RT-QPCR

Liver tissue was homogenised in Trizol (Life Technologies). Homogenates were mixed with chloroform (1:5 ratio Chloroform:Trizol) and centrifuged at 4°C, 1'200g, for 15 minutes. The aqueous supernatant was removed and mixed 1:1 with 70% ethanol. RNA was extracted using a Qiagen RNaesy mini kit according to the manufacturer's instructions. Reverse Transcription and Real Time-QPCR was performed using Qiagen Quantitect and Quantifast reagents on a LightCycler 480 II (Roche). Commercial primers from Qiagen's Quantitect range were used; Cdkn1a (Qiagen QT00137053), Igfbp1 (Qiagen QT001114716), Tgfb1 (Qiagen QT00145250), krt19 (Qiagen QT00156667), β1-Integrin (Qiagen, QT00155855) and Peptidylprolyl isomerase A (PPIA) (Qiagen QT00247709). Gene expression was normalised to the house keeping gene, PPIA. Samples were run in triplicate. The RT^2 Profiler PCR Array, Drug Metabolism: Phase I Enzymes was purchased from Qiagen (330231 PAMM-068Z), cDNA was synthesised from extracted RNA using the RT^2 First stand Kit (Qiagen; 330401) according to the manufactures instructions. The RT^2 Profiler

PCR Array was run on a Roche LightCycler 480 II with RT^2 SYBR Green qPCR Mastermix (Qiagen; 330500), according to the manufactures instructions. Analysis were performed according to manufacturer's templates and guidelines.

Whole Genome RNA sequencing

Samples were treated with DNase (Ambion), and sample integrity verified on the Agilent Bioanalyser with the RNA Nano chip. Illumina Tru-seq paired end strand specific sequencing (Illumina, USA) was carried out on a NextSeq-550 sequencer (Edinburgh Clinical Research Facility, Western General Hospital, Edinburgh, Scotland, UK). 500ng of Total RNA underwent ribosomal RNA depletion (rRNA) prior to purification, fragmentation, random hexamer cDNA generation and purification with AMPure XP beads (Beckman-Coulter, USA). Multiple indexing adapters were ligated to ds cDNA with subsequent hybridisation onto flow cells, and DNA fragment enrichment by 15 cycle PCR for sequencing. Completed libraries were quantified by qPCR using the KAPA Illumina Library Quantification Kit (Illumina, USA) before multiplexing in two equimolar pools and running on two flow cells on the Illumina NextSeq 550. The resulting FastQ files were mapped to the reference genome (mm9) using the Tophat alignment tool (V2) on Illumina Basespace software and reads per kilobase per million (RPKM) scores calculated for each gene. Differential gene expression was carried out using DEseq with cut offs of Log2 fold change >2 and adjusted P values <0.05 within replicates applied. Global analysis of total RPKM datasets to assess overall transcriptional states was carried out by calculating and plotting Pearson's correlation scores visualized as a heat map with Euclidian and Ward clustering applied. PCA plots were also carried out with the use of Illumina Basespace software. Plots for Pearson's correlation scores with hierarchical clustering were also carried out on all genes displaying significant gene expression changes relative to the control set. Visual examples of the transcriptional data were generated by calculating the average expression per group (control, $\beta 1$ $integrein^{fl/fl}$, AAV8-p21 & Biliary Duct) and loading onto the Broad Institute's Integrative Genomics Browser (https://software.broadinstitute.org/software/igv/download). RPKM values for select gene sets (hepatocyte, biliary, Notch signaling and Wnt signaling) were also clustered by Euclidian and Ward methods and expression patterns visualized by plotting as a Z-score heatmap with row normalized values. Data files can be accessed through GEO, with the following accession number GSE98034.

Statistical Analysis

Prism software (GraphPad Software, Inc) was used for all statistical analysis. Data is presented as mean ± s.e.m. n refers to biological replicates. Normal distribution of data was determined using D'Agostino and Pearson omnibus normality test. For parametric data, data significance was analysed using a two-tailed unpaired Students t-test. In cases where more than two groups were being compared, then a one-way ANOVA was used. In cases where two groups were split between two independent variables a two-way ANOVA was used. In instances where the n was too small to determine normal distribution or the data was non-parametric then a two-tailed Mann Whitney U-test was used. F tests were used to compare variances between groups.

In cases which randomisation was used (including animal studies), samples were randomized by a 'blinded' third party before being assessed separate 'blinded' assessor. Unblinding was performed immediately prior to final data analysis.

Serum analysis

Serum analysis used commercial kits according to the manufacturer's instructions; alanine transaminase, albumin, bilirubin (Alpha Laboratories); aspartate aminotransferase and alkaline phosphatase (Randox laboratories). All kits were adapted for use on a Cobas Fara centrifugal analyser (Roche).

Reproducibility of experiments

Routinely qPCR experiments were performed in technical triplicates of multiple biological replicates. For representative images 3-4 liver lobes were examined histologically in at least 3 biological replicates; further details referring to the specific numbers of biological replicates for each experiment can be found in the figure legend.

Europe PMC Funders Author Manuscripts

Europe PMC Funders Author Manuscripts

Extended Data

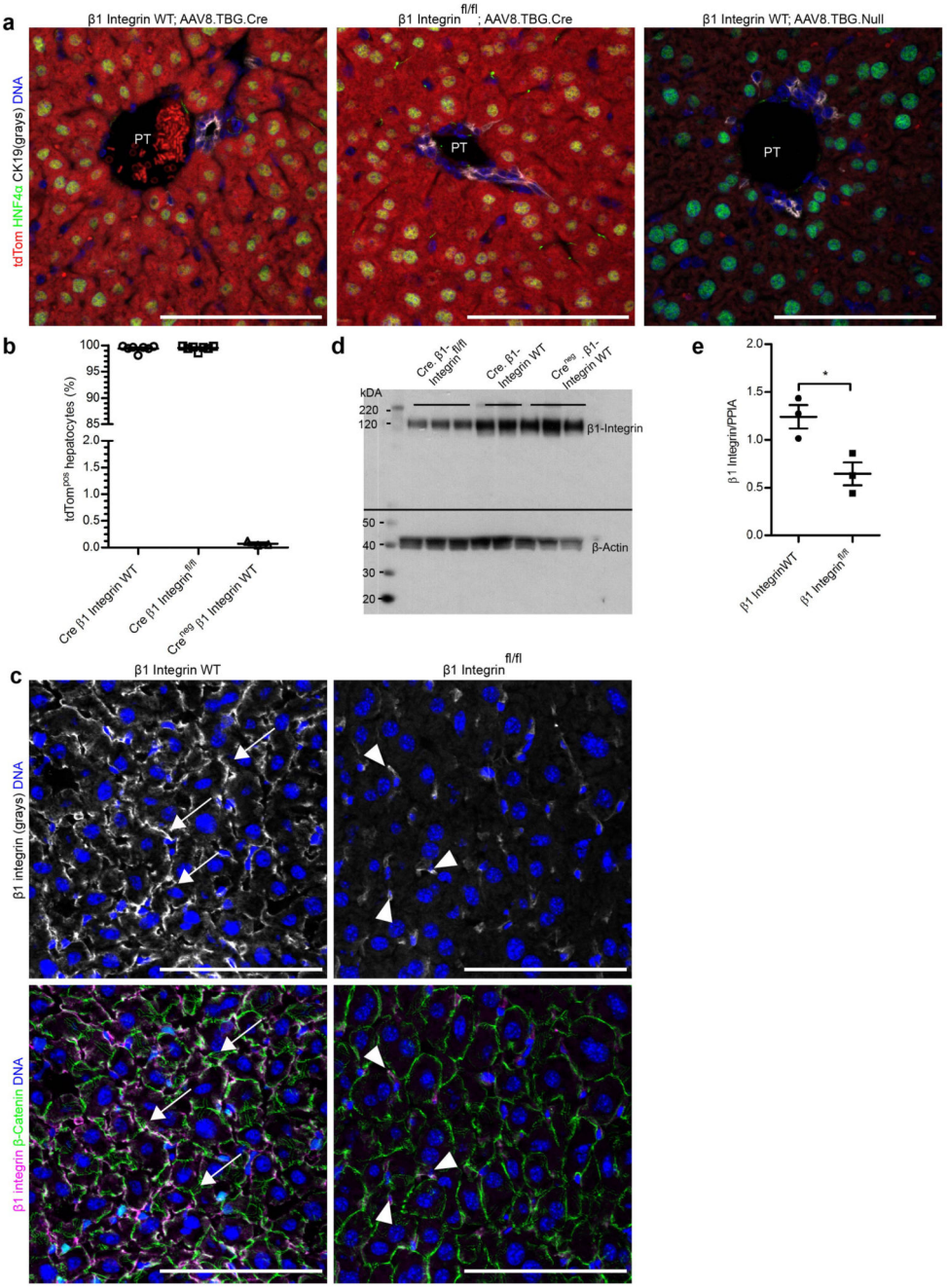

Extended Data Figure 1. AAV8.TBG.Cre labelled and deleted β1-Integrin in 99.5% of hepatocytes.

a, tdTom, biliary specific cytokeratin 19 (CK19) and hepatocyte specific HNF4α immunofluorescence in AAV8.TBG.Cre/null treated livers 2 weeks post AAV administration. Cre treated HNF4α^{pos} hepatocytes are tdTom^{pos} in contrast to the null treated; CK19^{pos} ductal cells are located at the portal tract (PT), confocal images. **b**, Liver tissue analysis quantifying tdTom^{pos}, HNF4α^{pos} hepatocytes 2 weeks post AAV8.TBG.Cre/

null administration, AAV8.TBG.Cre *n*=7, AAV8.TBG.null *n*=3. **c**, Hepatocellular β1-Integrin immunofluorescence grayscale image and dual image with membranous β-catenin, 2 weeks post AAV8.TBG.Cre administration, arrows identify β1-Integrin in the hepatocyte cell membrane, arrowheads identify non-parenchymal β1-Integrin staining; confocal images. **d**, 2 weeks post AAV8.TBG.Cre administration; whole liver β1-Integrin Western Blot. **e**, 2 weeks post AAV8.TBG.Cre administration; whole liver QPCR for β1-Integrin, *n*=3. *n*=number of mice per group, experiment was repeated twice. Scale bars: 100μM. Data are mean ± s.e.m.; two-tailed unpaired t-test; * P=0.05.

Europe PMC Funders Author Manuscripts

Europe PMC Funders Author Manuscripts

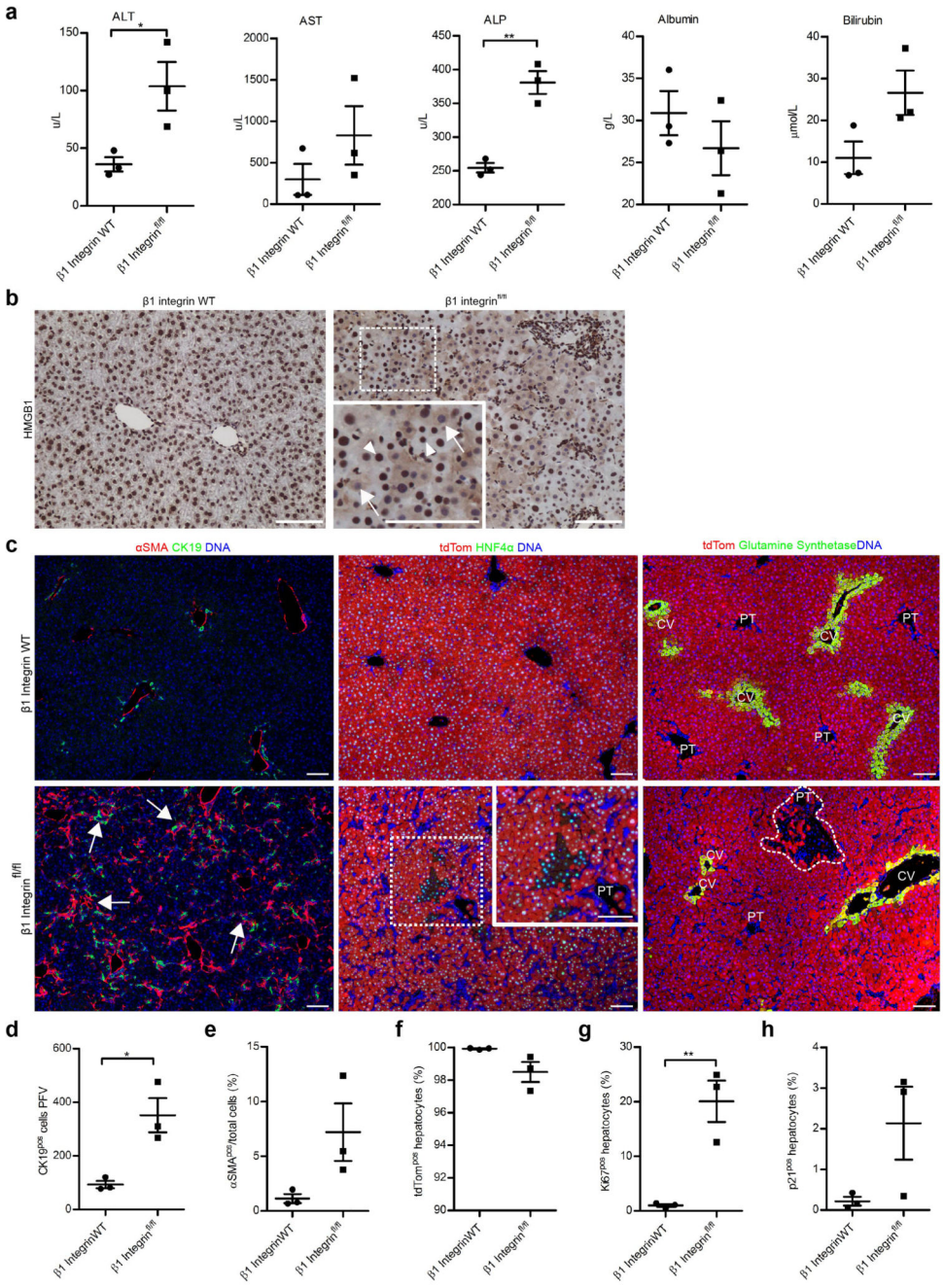

Extended Data Figure 2. Ablation of β1-Integrin caused liver damage, ductular reaction and small patches of un-labelled periportal hepatocytes.

a, Serum ELISA for markers associated with liver function 9 weeks post AAV8.TBG.Cre administration; *n*=3. **b,** 9 weeks post AAV8.TBG.Cre administration; anti-HMGB1 DAB immunohistochemistry. Arrowheads identify nuclear HMGB1, arrows highlight cytoplasmic HMGB1. **c**, 9 week post AAV8.TBG.Cre; α smooth muscle actin (αSMA)/CK19, tdTom/HNF4α and glutamine synthetase (GS)/tdTom immunofluorescence, arrows point to areas with DR. **d**, Liver tissue analysis quantifying $CK19^{pos}$ cells 9 weeks post AAV8.TBG.Cre

administration; *n*=3. **e**, Liver tissue analysis quantifying αSMA^{pos} cells 9 weeks post AAV8.TBG.Cre administration; *n*=3. **f**, Liver tissue analysis quantifying tdTom^{pos}, HNF4α^{pos} hepatocytes in livers 9 weeks post AAV8.TBG.Cre administration; *n*=3. **g**, Liver tissue analysis quantifying Ki67^{pos}, HNF4α^{pos} hepatocytes 9 weeks post AAV8.TBG.Cre administration; n=3. **h**, Liver tissue analysis quantifying p21^{pos}, HNF4α^{pos} hepatocytes 9 weeks post AAV8.TBG.Cre administration; *n*=3. *n*=number of mice per condition, the experiment was performed once. Scale bars: 100μM. Data are mean ± s.e.m.; two-tailed unpaired t-test; * P=0.05, ** P=0.01.

Europe PMC Funders Author Manuscripts

Europe PMC Funders Author Manuscripts

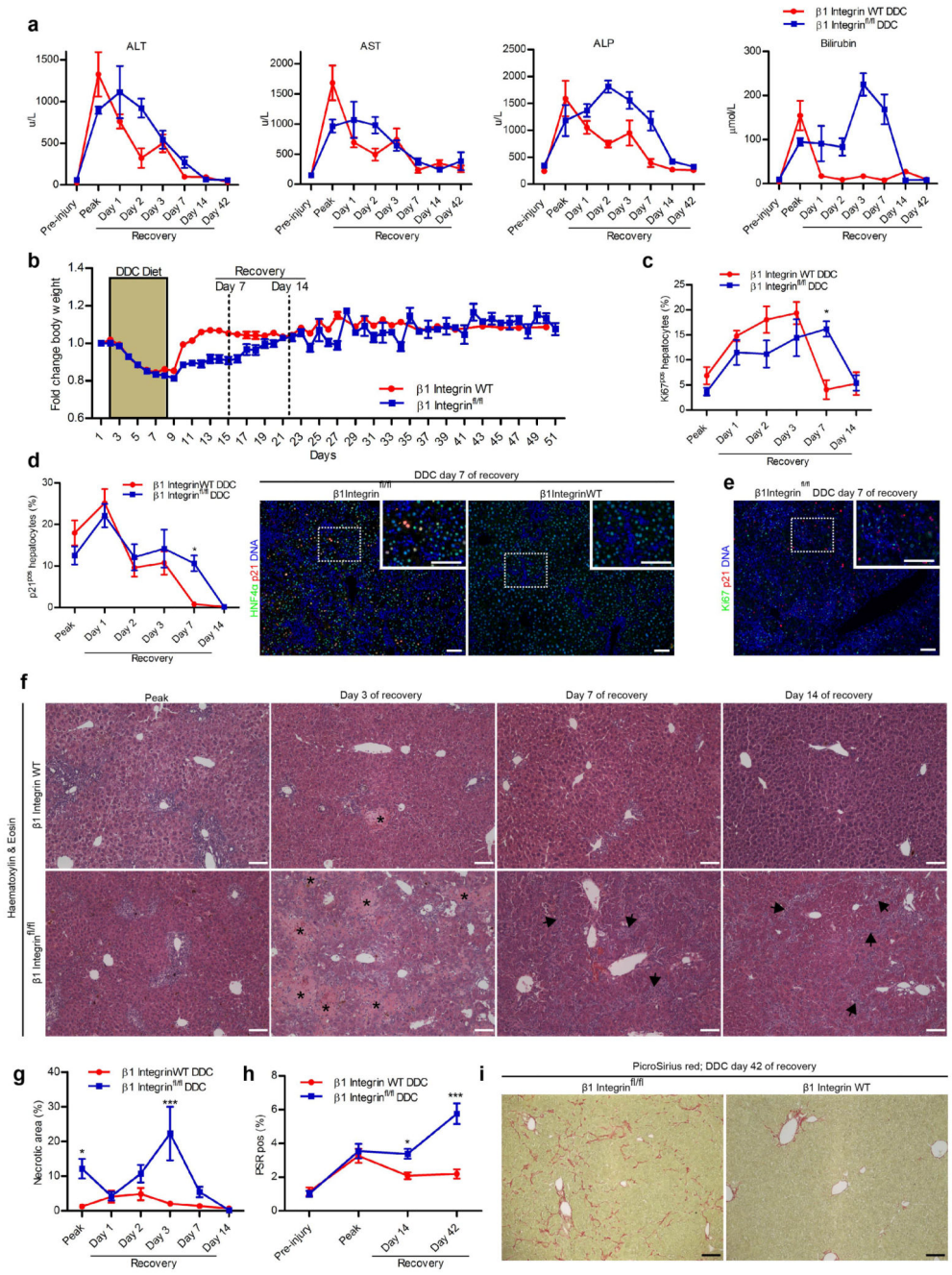

Extended Data Figure 3. Hepatocyte β1-Integrin deletion delayed and altered the regenerative response after treatment with the liver injury diet DDC.

a, DDC diet and recovery; serum ELISA for markers associated with liver function, n=5. **b** Body weight measurements during DDC diet and the subsequent recovery; n=5. **c**, Liver tissue analysis quantifying prolonged Ki67^{pos}/HNF4α^{pos} hepatocytes after DDC injury; n=5. **d**, Liver tissue analysis quantifying p21^{pos}/HNF4α^{pos} hepatocytes after DDC injury; n=5, and representative p21/HNF4α immunofluorescence in samples 7 days after DDC injury. **e**, p21/Ki67 immunofluorescence 7 days after DDC injury. **f**, Representative

Haematoxylin & Eosin (H&E) histochemical stain of sections after DDC injury; asterisks highlight necrotic areas; arrows highlight small cellular infiltrate. **g**, Morphometric quantification of necrotic area from H&E sections in DDC treated samples at peak injury and recovery. **h**, fibrosis analysis, percentage of pixels PicroSirius Red (PSR) positive, before, during and after DDC injury; n=5, except pre-injury PSR which is n=3. **i**, Representative images of PSR histochemistry on samples from day 42 of recovery after DDC diet. n=number of mice per condition, the experiment was performed 1-2 times. Scale bars: 100μM. Data are mean ± s.e.m.; two-tailed unpaired t-test; 2way ANOVA, Bonferroni post-tests. * P=<0.05, ** P=<0.01, *** P=<0.001.

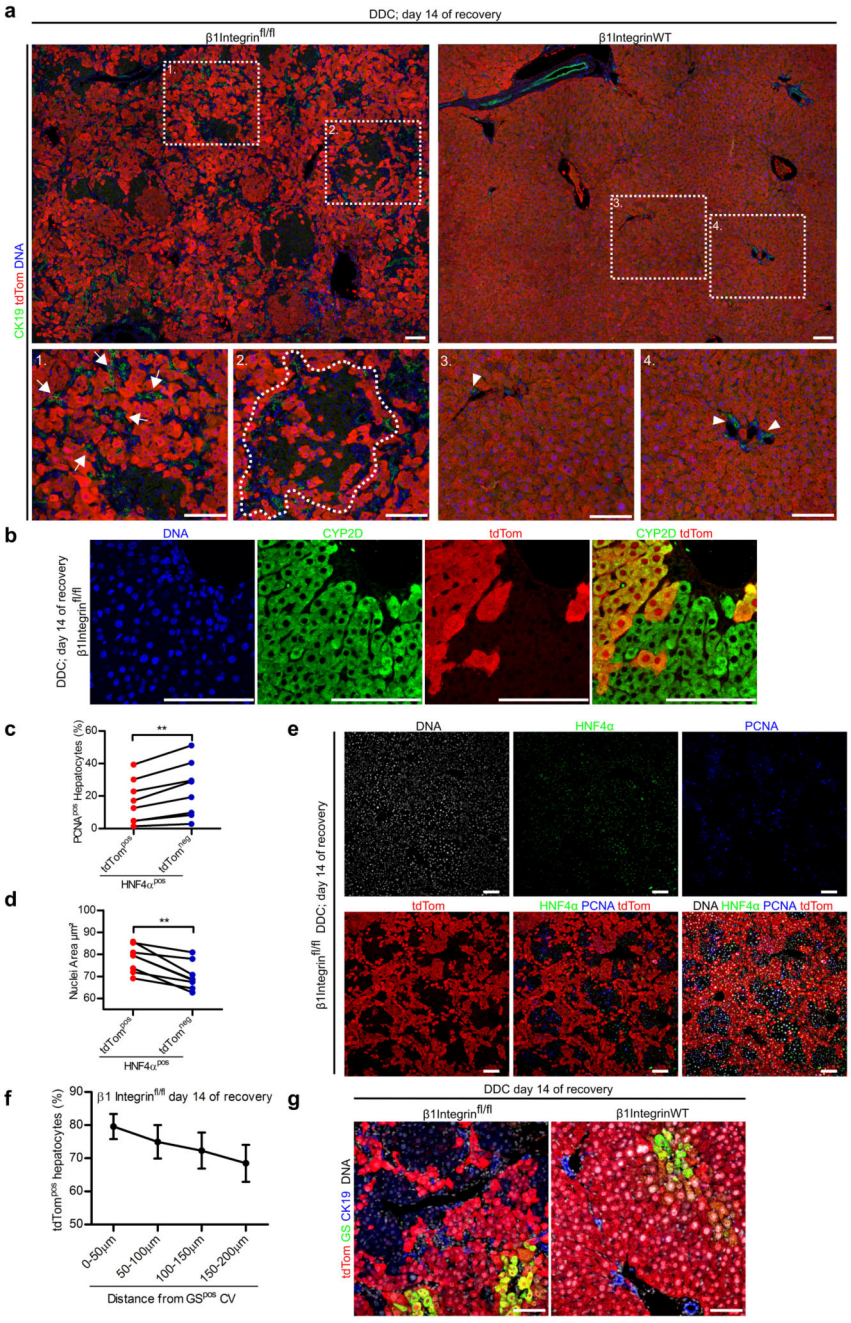

Extended Data Figure 4. β1-Integrin ablation and DDC induced injury resulted in large areas of tdTom^{neg} hepatocytes.

a, tdTom/CK19 immunofluorescence, tiled images of β1-Integrin$^{fl/fl}$ and β1-Integrin WT livers after DDC diet and 14 days of recovery. (1-4) Enlarged regions of interest; (1) invasive CK19 positive cells (arrows), (2) tdTom negative regenerative nodule, (3, 4) fully recovered β1-Integrin WT liver with typical biliary ducts (arrowheads). **b**, Separate channels from a merged CYP2D and tdTom immunofluorescent confocal image in Fig 1g, showing CYP2D expression between tdTom^{pos} and tdTom^{neg} hepatocytes. **c, d** and **e**, Liver tissue analysis and

a representative PCNA/HNF4α/tdTom immunofluorescent image in β1-Integrin$^{fl/fl}$ mice at day 14 recovery post DDC injury; quantifying PCNA expression and nucleus size in both tdTom^{pos} and tdTom^{neg} hepatocytes (HNF4α^{pos}); *n*=8 mice analysed, the experiment was performed once. **f**, Liver tissue analysis in β1-Integrin$^{fl/fl}$ mice at day 14 recovery post DDC injury; quantifying tdTom^{pos} HNF4α^{pos} hepatocytes adjacent to the GS^{pos} CV. *n*=7 mice analysed, the experiment was performed once. **g**, tdTom/GS/CK19 immunofluorescence in mice at day 14 recovery post DDC diet, β1-Integrin$^{fl/fl}$ liver has patches of tdTom^{neg} hepatocytes connected to CK19^{pos} biliary epithelium, tdTom^{pos} hepatocytes remain arranged around the GS^{pos} central veins (CV). Data are mean ± s.e.m.; ** P=<0.01, paired t-test.

Europe PMC Funders Author Manuscripts

Europe PMC Funders Author Manuscripts

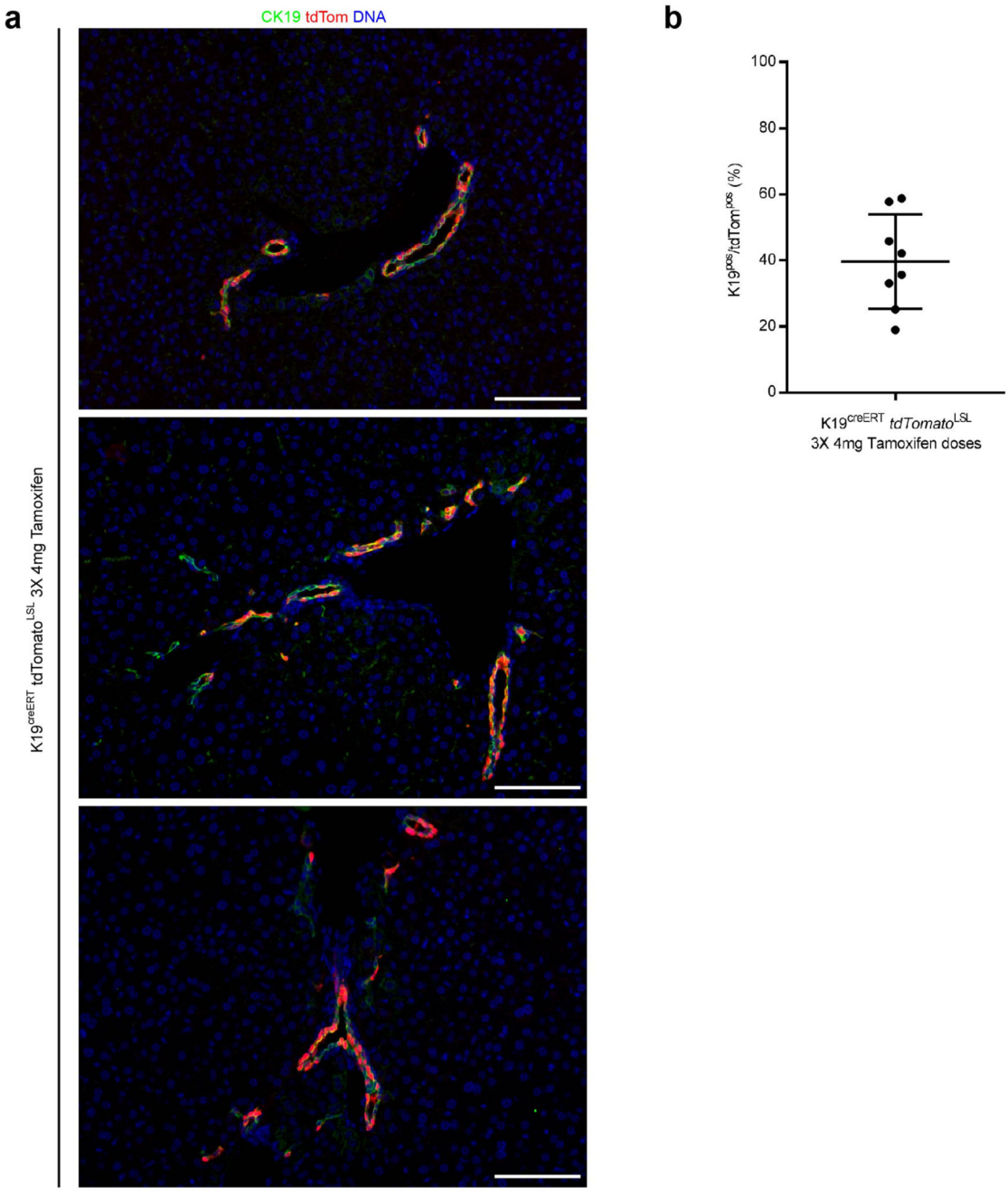

Extended Data Figure 5. K19^{CreERT} *tdTomato*^{LSL} strictly labels 40% of the biliary epithelium.
Three X 4mg doses of tamoxifen followed by a 14day wash out period. **a**. Representative images of CK19/tdTom dual immunofluorescence. **b**. Quantification of CK19pos biliary epithelial cells which are tdTomato positive n=8 mice analysed, the experiment was performed once.Scale Bars: 100μM. Data are shown as mean ± s.e.m.

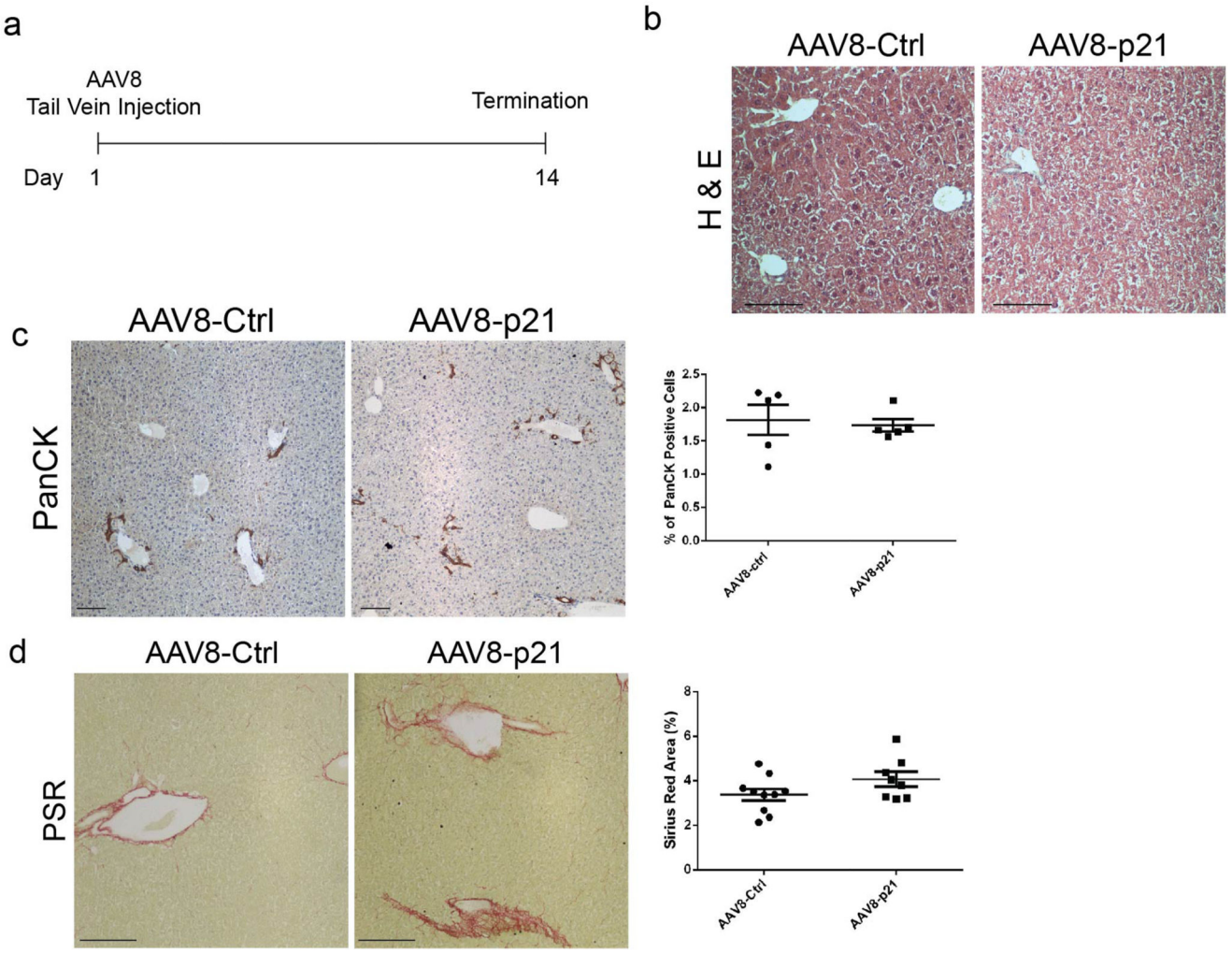

Extended Data Figure 6. Analysis of AAV8-p21 injected livers.

a. Schematic showing the experimental design of the AAV8-p21 injection. **b.** Haematoxylin and Eosin staining on the livers of AAV8 injected mice. **c.** Quantification and representative images of immunostaining for PanCK^{pos} cells of the AAV8 vectors injected liver. **d.** Picro Sirius Red analysis of the AAV8 vectors injected livers. Scale Bars: 100μM. *n*=5 mice. Experiments were performed twice. Data are shown as mean ± s.e.m. Mann-Whitney U-test, *P < 0.05

Europe PMC Funders Author Manuscripts

Europe PMC Funders Author Manuscripts

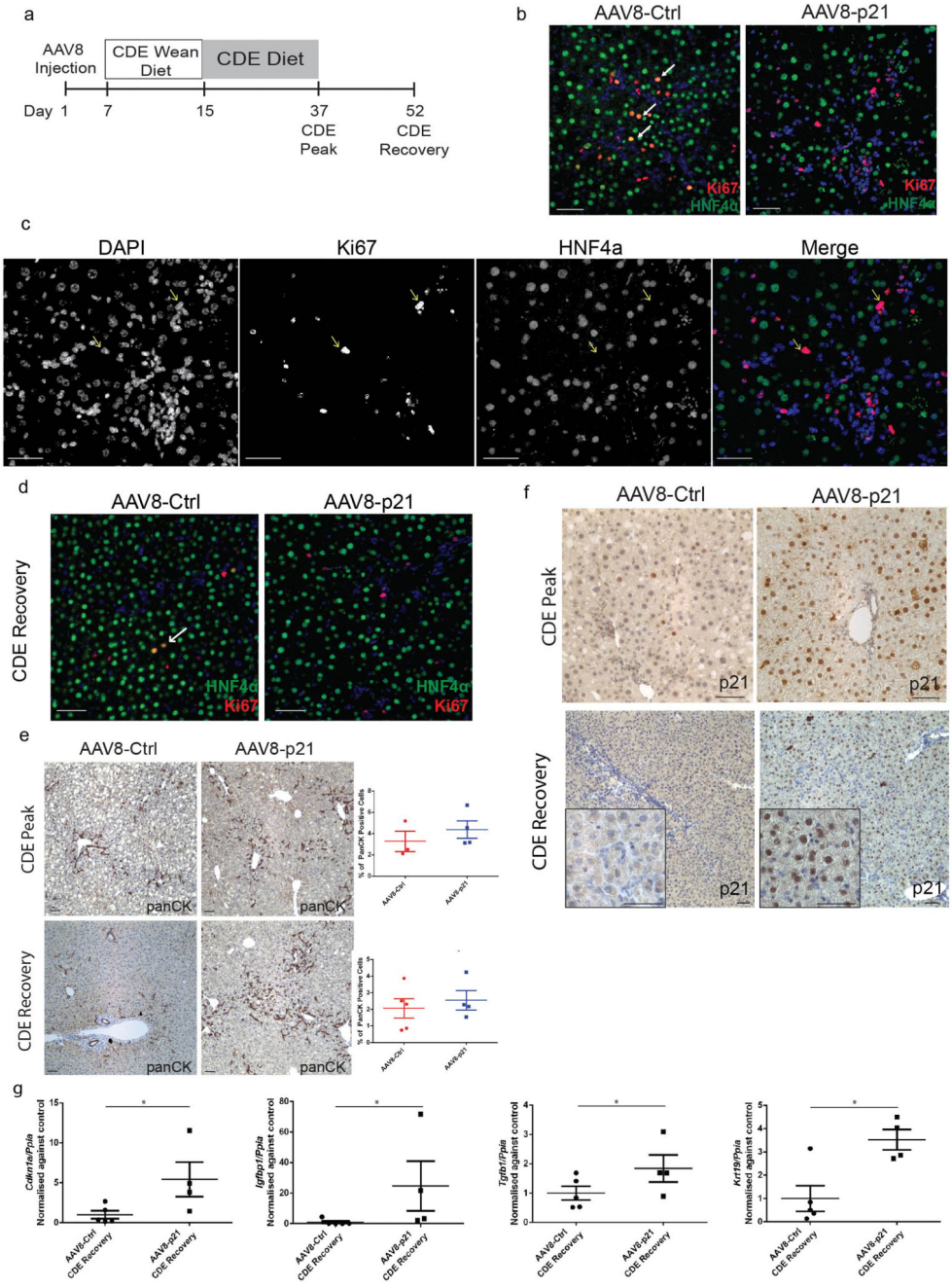

Extended Data Figure 7. Analysis of AAV8-p21 injected livers following CDE injury regime.

a. Schematic representation of the CDE recovery regime. **b.** Immunostaining of Ki67 (red), HNF4α (green) on AAV8 injected mice during CDE injury. White arrows denote Ki67 and HNF4α double positive hepatocytes. **c.** Split channel images of DAPI, Ki67, and HNF4α on liver sections of AAV8-p21 injected mice following CDE injury. **d.** Ki67 (red) and HNF4α (green) immunohistochemistry of the liver of mice injected with AAV8-p21 and control 2 weeks after CDE injury **e.** PanCK immunohistochemistry and quantification of PanCK^{pos} cells of the liver of AAV8 injected mice during and 2 weeks after CDE diet induced injury. **f.**

p21 immunohistochemistry on AAV8 injected mice during and after CDE injury. Insets showing high magnification images. **g.** Whole liver *Cdkn1a, Igfbp1, Tgfb1, Krt19* mRNA expression of AAV8 vectors injected mice 2 weeks following CDE injury. Scale Bars: 100μM. *n*=4 mice. Experiments were performed once. Data are shown as mean ± s.e.m. Mann-Whitney U-test, *P < 0.05

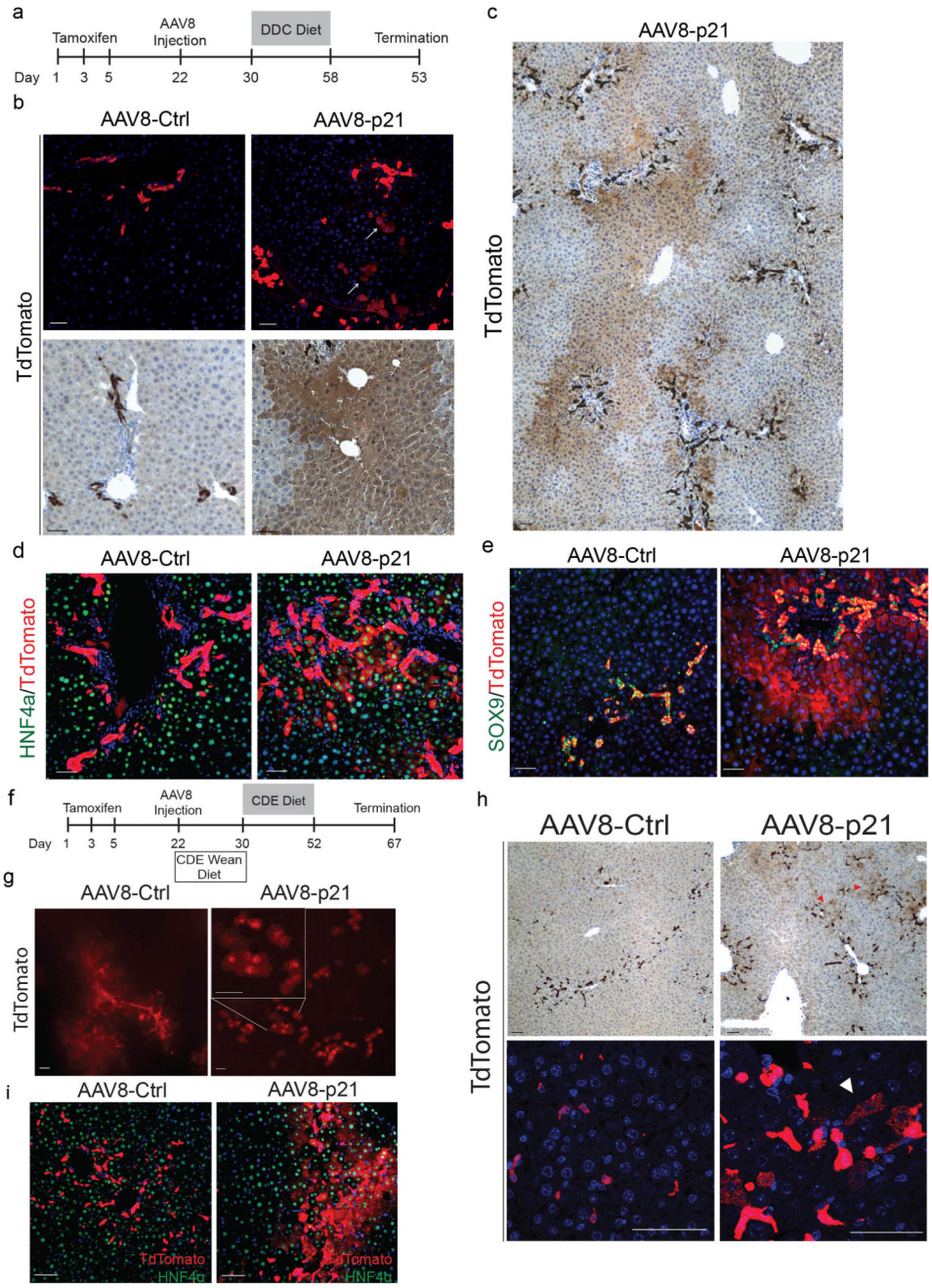

Extended Data Figure 8. Analysis of the Krt19^{Cre}tdTomato^{LSL} mice which received AAV8-p21 injection followed by DDC or CDE recovery regime.

Europe PMC Funders Author Manuscripts

a. Schematic showing the experimental design of the AAV8-p21 injection followed by DDC recovery regime. **b,c.** tdTom staining of $Krt19^{Cre}$ $tdTomato^{LSL}$ mice that received AAV8-p21 injection followed by DDC recovery regime. **d.** HNF4α (Green) and tdTom (red) staining on the $Krt19^{Cre}tdTomato^{LSL}$ mice that received AAV8 injections and treated with the DDC recovery regime. **e.** SOX9 (Green) and tdTom (red) staining on the $Krt19^{Cre}$ $tdTomato^{LSL}$ mice that received AAV8 injections and treated with the DDC recovery regime. **f**. Schematic representation of the experimental design of the AAV8-p21 injection followed by CDE recovery regime. **g**. Epifluorescence images of the liver of the mice received AAV8-ctrl or AAV8-p21 injections followed by the CDE recovery regime. **h**. Immunostaining for tdTomato of mice received AAV8-ctrl or AAV8-p21 injections followed by the CDE recovery regime. **i**. tdTomato (red) and HNF4α (green) immunofluorescent double staining of mice received AAV8-ctrl or AAV8-p21 injections followed by the CDE recovery regime. n=4 mice, experiments were performed once. Scale Bars: 100μM.

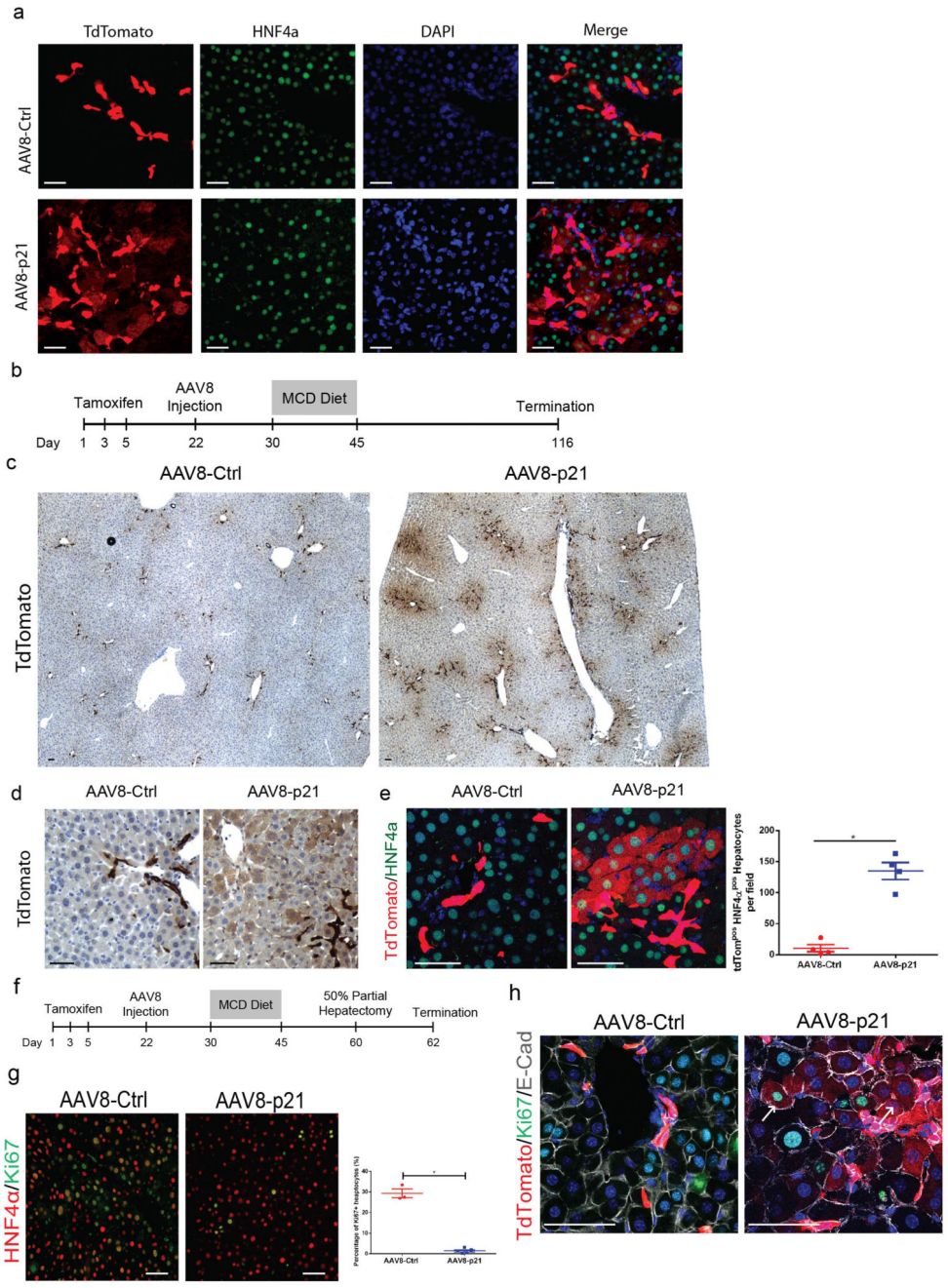

Extended Data Figure 9. Analysis of the Krt19^{Cre} tdTomato^{LSL} mice which received AAV8-p21 injection followed by MCD recovery regime.

a. Representative immunofluorescent images showing split channels of tdTomato, HNF4α, and DAPI of mice received AAV8-ctrl or AAV8-p21 injections followed by the MCD recovery regime. **b**. Schematic representation showing the experimental design of the AAV8-p21 injection followed by a MCD long recovery regime. **c,d**. tdTom staining of Krt19^{Cre} tdTomato^{LSL} mice that received AAV8-p21 injection followed by MCD long recovery regime. **e**. tdTomato (red) and HNF4α (green) immunofluorescent double staining and

quantification of tdTom^{pos} HNF4α^{pos} hepatocytes in that mice received AAV8-ctrl or AAV8-p21 injections followed by the MCD long recovery regime. **f**. Schematic representation of partial hepatectomy performed after the MCD recovery regime. **g**. Quantification and Immunofluorescent double staining of HNF4α (red), and Ki67(green) of mice received 50% partial hepatectomy. **h**. Confocal microscopy images of mice received 50% partial hepatectomy. tdTomato (red), Ki67 (green), E-Cadherin (grey). *n*=4 mice. Experiments were performed twice. Scale Bars: 100μM. Data are shown as mean ± s.e.m.

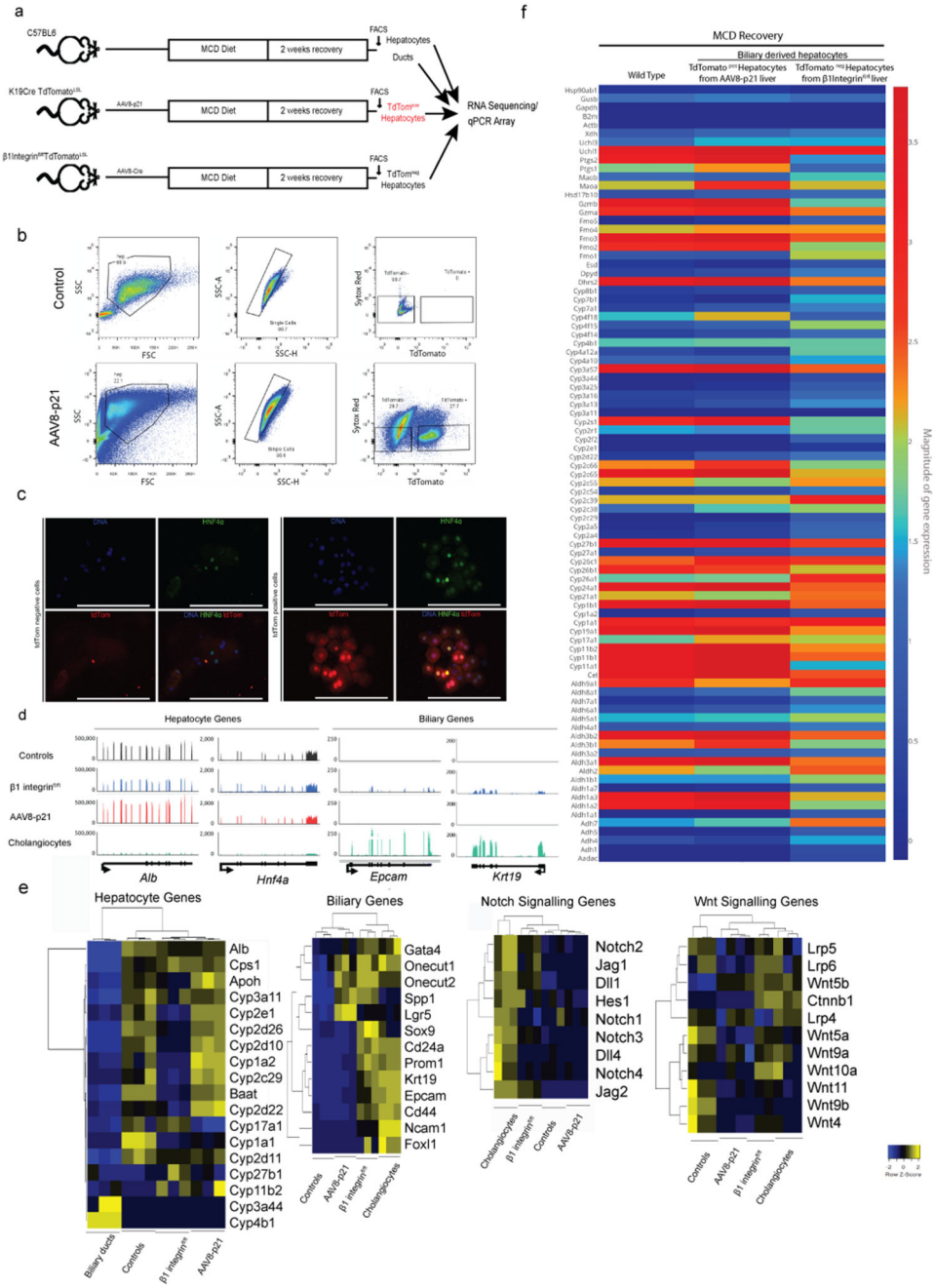

Europe PMC Funders Author Manuscripts

Europe PMC Funders Author Manuscripts

Extended Data Figure 10. Comparison between ductular derived hepatocytes and hepatocytes regenerated through self-duplication.

a. Experimental design to isolate wildtype hepatocytes/ducts and ductular derived hepatocytes from a regenerated liver. **b**. FACS gating strategy to isolate $tdTom^{pos}$ and $tdTom^{neg}$ hepatocytes. **c**. Cytospins and tdTom/HNF4α immunofluorescence of FACS sorted cells. **d**. Visual examples of average RNA-seq transcriptional reads in sample groups across select loci. Scales referring to normalised read counts are displayed on the right of each plot. RNAseq annotated genes are plotted n black below. **e**. RNAseq generated Z-score heatmaps with hierarchical clustering across specific gene sets. Heatmaps display gene expression levels normalised to each gene, yellow = higher expression, blue = lower expression, N=3. **f**. qPCR array for phase 1 drug metabolism enzymes n=3 mice. Experiments were performed once. Scale Bars: 100μM.

Acknowledgments

The authors would like to thank B. Vernay for assistance with microscopy, F. Rossi, C. Cryer with FACS, Prof Sabine Werner for advice, and Dr Frederic Mushinski for providing the p21 plasmid. Work in the lab of RRM was supported by the MRC(Ref:MC_PC_U127574433). This work was supported by the UK Medical Research Council (Ref:MR/L012766/1, MR/K017047/1) and the UK Regenerative Medicine Platform(Ref:MR/K026666/1).

References

1. Richardson MM, et al. Progressive Fibrosis in Nonalcoholic Steatohepatitis: Association With Altered Regeneration and a Ductular Reaction. Gastroenterology. 2007; 133:80–90. [PubMed: 17631134]
2. Marshall A, et al. Relation between hepatocyte G1 arrest, impaired hepatic regeneration, and fibrosis in chronic hepatitis C virus infection. Gastroenterology. 2005; 128:33–42. [PubMed: 15633121]
3. Yanger K, et al. Adult Hepatocytes Are Generated by Self-Duplication Rather than Stem Cell Differentiation. Cell Stem Cell. 2014; 19:340–349.
4. Schaub JR, Malato Y, Gormond C, Willenbring H. Report Evidence against a Stem Cell Origin of New Hepatocytes in a Common Mouse Model of Chronic Liver Injury. CellReports. 2014; 8:933–939.
5. Tarlow BD, Finegold MJ, Grompe M. Clonal tracing of Sox9+ liver progenitors in mouse oval cell injury. Hepatology. 2014; 60:278–289. [PubMed: 24700457]
6. Michalopoulos GK, Khan Z. Liver stem cells: Experimental findings and implications for human liver disease. Gastroenterology. 2015; :1–7. DOI: 10.1053/j.gastro.2015.08.004
7. Lu W-Y, et al. Hepatic progenitor cells of biliary origin with liver repopulation capacity. Nat Cell Biol. 2015; 17:971–983. [PubMed: 26192438]
8. Huch M, et al. In vitro expansion of single Lgr5+ liver stem cells induced by Wnt-driven regeneration. Nature. 2013; 494:247–50. [PubMed: 23354049]
9. He J, Lu H, Zou Q, Luo L. Regeneration of liver after extreme hepatocyte loss occurs mainly via biliary transdifferentiation in zebrafish. Gastroenterology. 2014; 146:789–800.e8. [PubMed: 24315993]
10. Petersen BE, Zajac VF, Michalopoulos GK. Hepatic oval cell activation in response to injury following chemically induced periportal or pericentral damage in rats. Hepatology. 1998; 27:1030–1038. [PubMed: 9537443]
11. Bird TG, Lorenzini S, Forbes SJ. Activation of stem cells in hepatic diseases. Cell Tissue Res. 2008; 331:283–300. [PubMed: 18046579]
12. Lin W-R, et al. The histogenesis of regenerative nodules in human liver cirrhosis. Hepatology. 2010; 51:1017–1026. [PubMed: 20198634]
13. Yanger K, et al. Robust cellular reprogramming occurs spontaneously during liver regeneration. Genes Dev. 2013; 27:719–724. [PubMed: 23520387]

14. Font-Burgada J, et al. Hybrid Periportal Hepatocytes Regenerate the Injured Liver without Giving Rise to Cancer. Cell. 2015; 162:766–779. [PubMed: 26276631]
15. Shin S, Upadhyay N, Greenbaum LE, Kaestner KH. Ablation of Foxl1-Cre–Labeled Hepatic Progenitor Cells and Their Descendants Impairs Recovery of Mice From Liver Injury. Gastroenterology. 2015; 148:192–202.e3. [PubMed: 25286440]
16. Español-Suñer R, et al. Liver progenitor cells yield functional hepatocytes in response to chronic liver injury in mice. Gastroenterology. 2012; 143:1564–1575.e7. [PubMed: 22922013]
17. Raghavan S, Bauer C, Mundschau G, Li Q, Fuchs E. Conditional ablation of β1 integrin in skin: Severe defects in epidermal proliferation, basement membrane formation, and hair follicle invagination. J Cell Biol. 2000; 150:1149–1160. [PubMed: 10974002]
18. Speicher T, et al. Knockdown and knockout of β1-integrin in hepatocytes impairs liver regeneration through inhibition of growth factor signalling. Nat Commun. 2014; 5:3862. [PubMed: 24844558]
19. Huebener P, et al. The HMGB1/RAGE axis triggers neutrophil-mediated injury amplification following necrosis. J Clin Invest. 2015; 125:539–550. [PubMed: 25562324]
20. Liu Y, et al. Animal models of chronic liver diseases. Am J Physiol Gastrointest Liver Physiol. 2013; 304:G449–68. [PubMed: 23275613]
21. Bogorad RL, et al. Nanoparticle-formulated siRNA targeting integrins inhibits hepatocellular carcinoma progression in mice. Nat Commun. 2014; 5:3869. [PubMed: 24844798]
22. Huppi K, et al. Molecular cloning, sequencing, chromosomal localization and expression of mouse p21 (Waf1). Oncogene. 1994; 9:3017–3020. [PubMed: 8084607]
23. Wang B, Zhao L, Fish M, Logan CY, Nusse R. Self-renewing diploid Axin2+ cells fuel homeostatic renewal of the liver. Nature. 2015; doi: 10.1038/nature14863
24. Planas-Paz L, et al. The RSPO–LGR4/5–ZNRF3/RNF43 module controls liver zonation and size. Nat Cell Biol. 2016; doi: 10.1038/ncb3337
25. Mitchell C, Willenbring H. A reproducible and well-tolerated method for 2/3 partial hepatectomy in mice. Nat Protoc. 2008; 3:1167–1170. [PubMed: 18600221]
26. Preibisch S, Saalfeld S, Tomancak P. Globally optimal stitching of tiled 3D microscopic image acquisitions. Bioinformatics. 2009; 25:1463–1465. [PubMed: 19346324]
27. Kreamer BL, et al. Use of a low-speed, iso-density percoll centrifugation method to increase the viability of isolated rat hepatocyte preparations. Vitr Cell Dev Biol. 1986; 22:201–211.

Europe PMC Funders Author Manuscripts

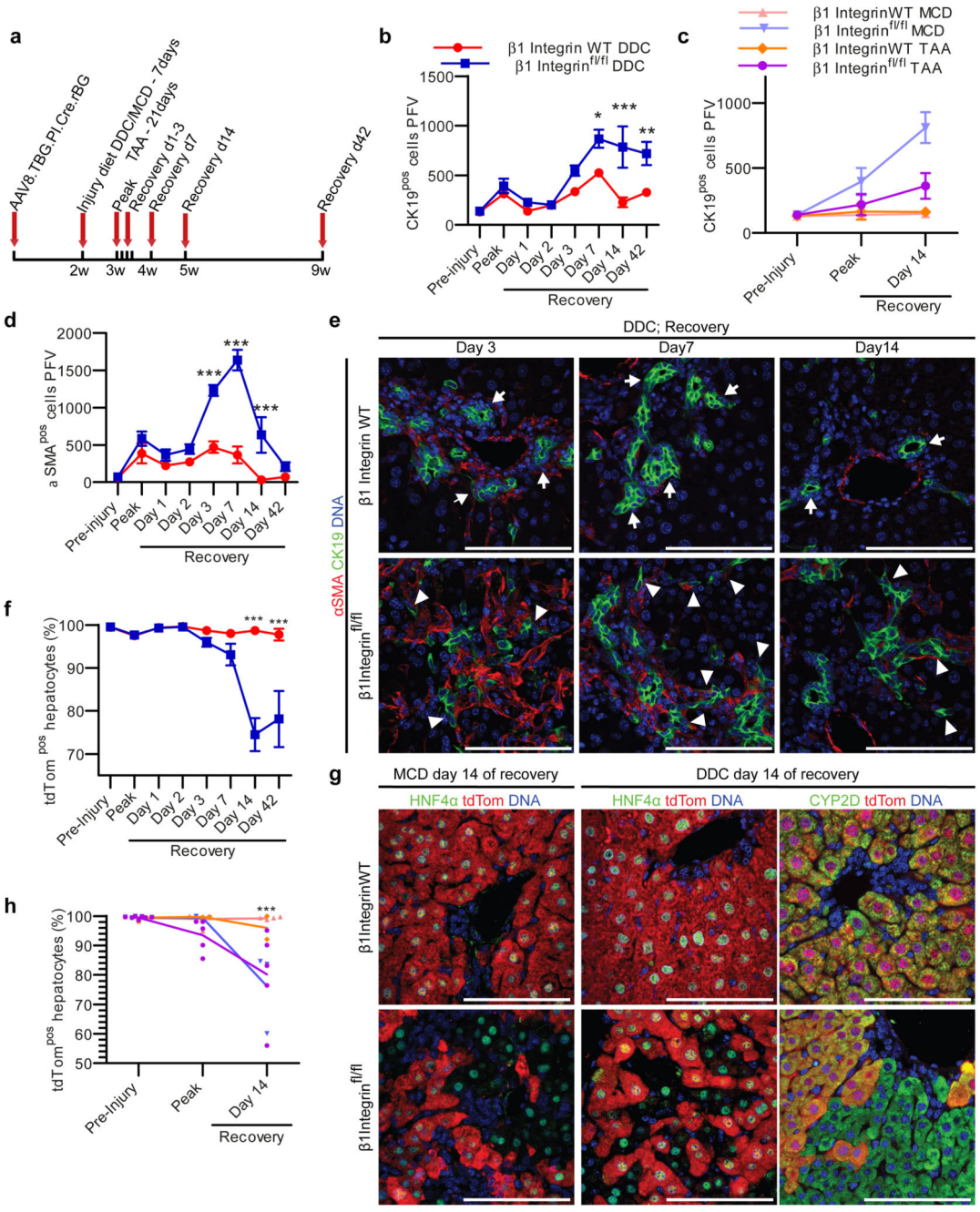

Figure 1. Hepatocyte β1-Integrin ablation combined with liver injury amplifies ductular reaction and hepatocytes regenerate from a non-hepatocyte source.

a, Experimental strategy to stimulate liver regeneration with hepatotoxic agents. **b-d**, Quantification of CK19^{pos} cells or αSMA^{pos} cells; before, during and after injury (n=5 DDC, n=3 MCD and n=2 TAA; n=3 for preinjury αSMA analysis. **e**, Confocal CK19/ αSMA immunofluorescence; invasive biliary cells(arrowheads), ducts with lumens(arrows). **f,h**, Quantification of tdTom^{pos}/HNF4α^{pos} hepatocytes before, during and after injury (n=5 DDC, n=3 MCD and n=2 TAA). **g** Confocal tdTom immunofluorescence of CYP2D and

HNF4α hepatocytes. PFV-per field of view. *n*=number of mice per condition; experiments were performed 1-2 times. Scale bars:100μM. Data are mean ± s.e.m.; * P=<0.05; ** P=<0.01; *** P=<0.001; 2way ANOVA, Bonferroni post-tests.

Europe PMC Funders Author Manuscripts

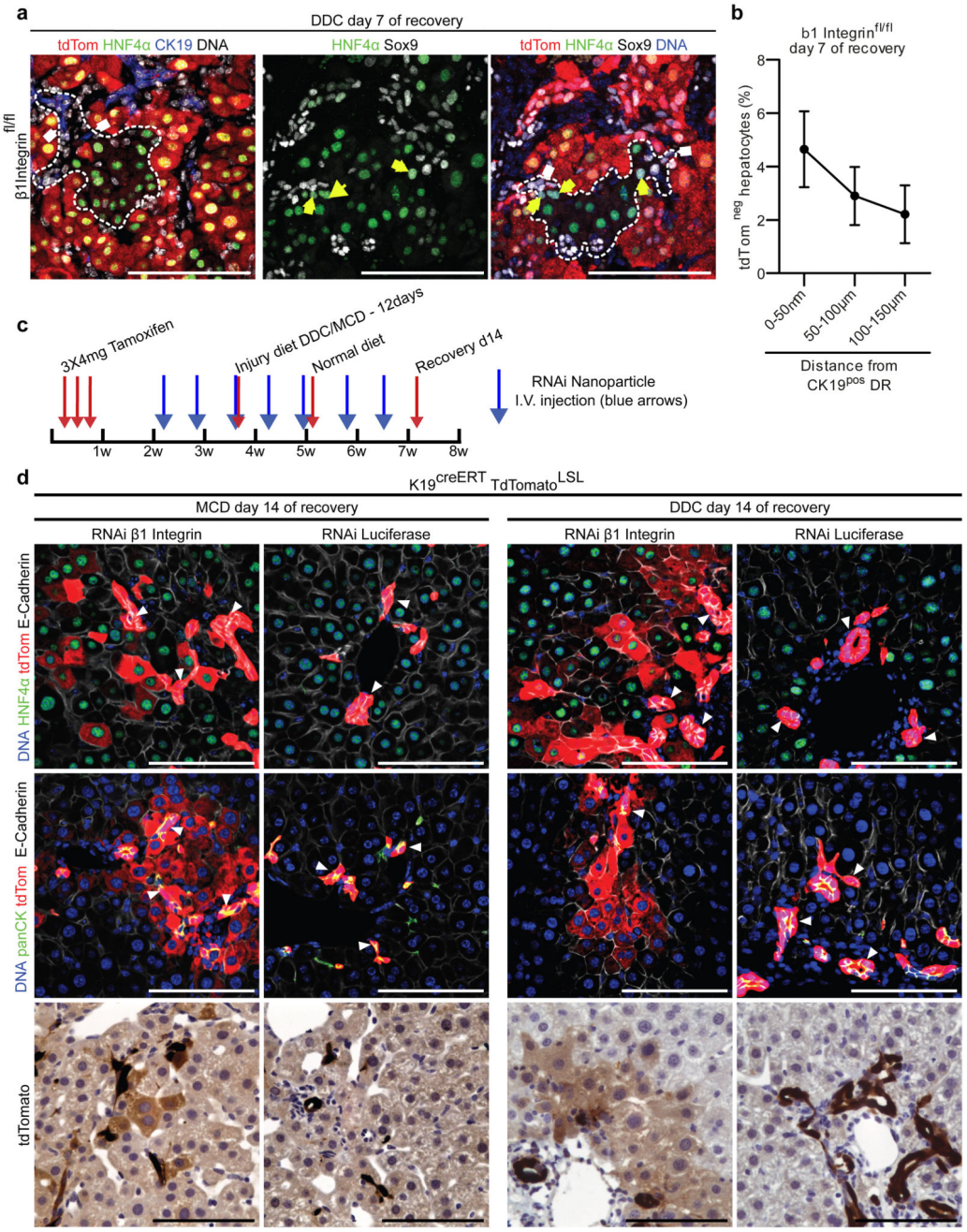

Figure 2. Non-hepatocyte derived hepatocytes originated from the portal tract, Keratin19 biliary lineage tracing confirmed their ductal origin.

a, tdTom /HNF4α/CK19 and tdTom/HNF4α/Sox9 immunofluorescent confocal images at day 7 recovery post DDC diet. tdTom^{neg} hepatocytes(HNF4α^{pos}) adjacent to CK19^{pos} and Sox9^{pos} ductular reactions (white arrows) and rare tdTom^{neg} hepatocytes Sox9^{pos}/ HNF4α^{pos}(yellow arrows). **b**, Quantification of tdTom^{neg}/HNF4α^{pos} hepatocytes adjacent to the CK19^{pos} DRs post DDC injury; n=6 mice analysed, the experiment was performed twice. **c,** Experimental strategy to lineage trace biliary epithelial cells on a background of

liver injury and hepatocyte *Itgβ1* silencing. **d**, Immunofluorescent confocal images and immunohistochemistry 14 days after DDC and MCD diet combined with RNAi mediated β1 Integrin or luciferase mRNA suppression, bile ducts(arrowheads). Images are representative of $n = 4$ mice per condition, experiments were performed once. Scale bars:100μM Data are mean ± s.e.m.

Europe PMC Funders Author Manuscripts

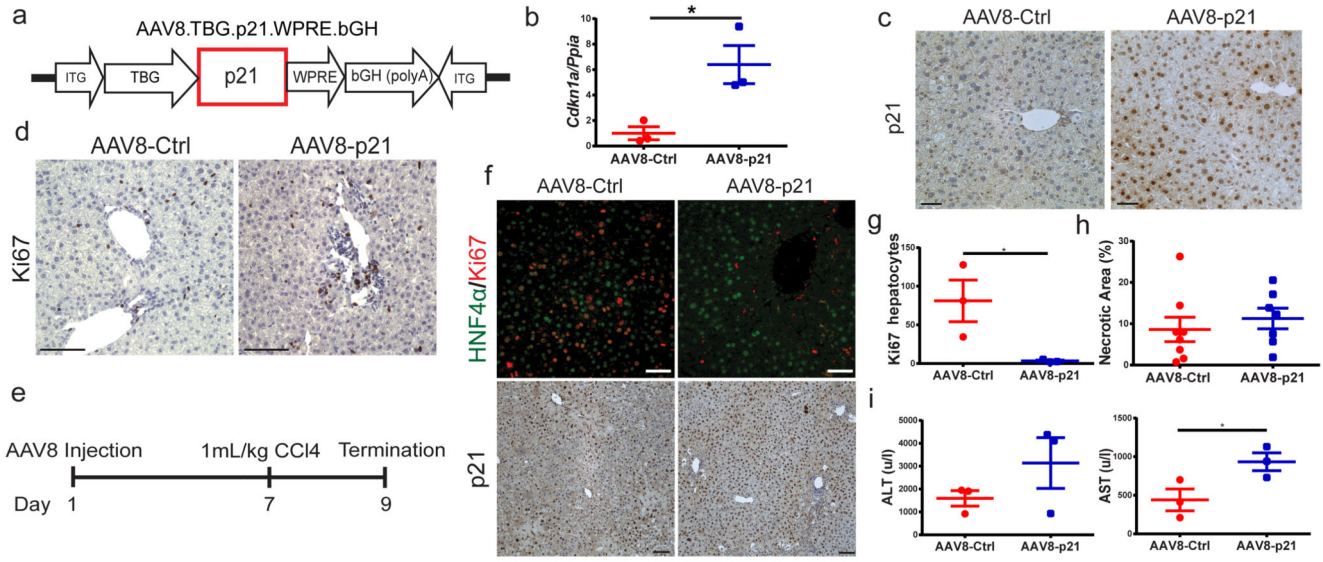

Figure 3. Inhibition of hepatocyte proliferation following AAV8-p21 injection.

a, Schematic representing the AAV8-p21 construct. **b,** *Cdkn1a* whole liver RNA expression after AAV8 injection. *n*=3 mice **c,** p21 immunohistochemistry of AAV8 injected mice. **d,** Ki67 immunostaining of AAV8 injected livers. **e,** Experimental design of the AAV8-p21 with CCl_4 regime. **f,** Ki67/HNF4α immunofluorescence following AAV8 and CCl_4 injection, upper panel. p21 immunohistochemistry following CCl_4 injection. **g,** Quantification of $Ki67^{pos}$ hepatocytes in mice injected with CCl_4 after AAV8 injection. *n*=3 mice **h,** Necrotic area 48-hours post CCl_4 injection *n*=7 mice **I,** Mouse serum ALT and AST after CCl_4. Scale bars:100μM. *n*=3 mice. Data are representative of 1-2 independent experiments. Experiments were performed twice. Data are shown as mean ± s.e.m. Mann-Whitney U-test *P < 0.05.

Europe PMC Funders Author Manuscripts

Europe PMC Funders Author Manuscripts

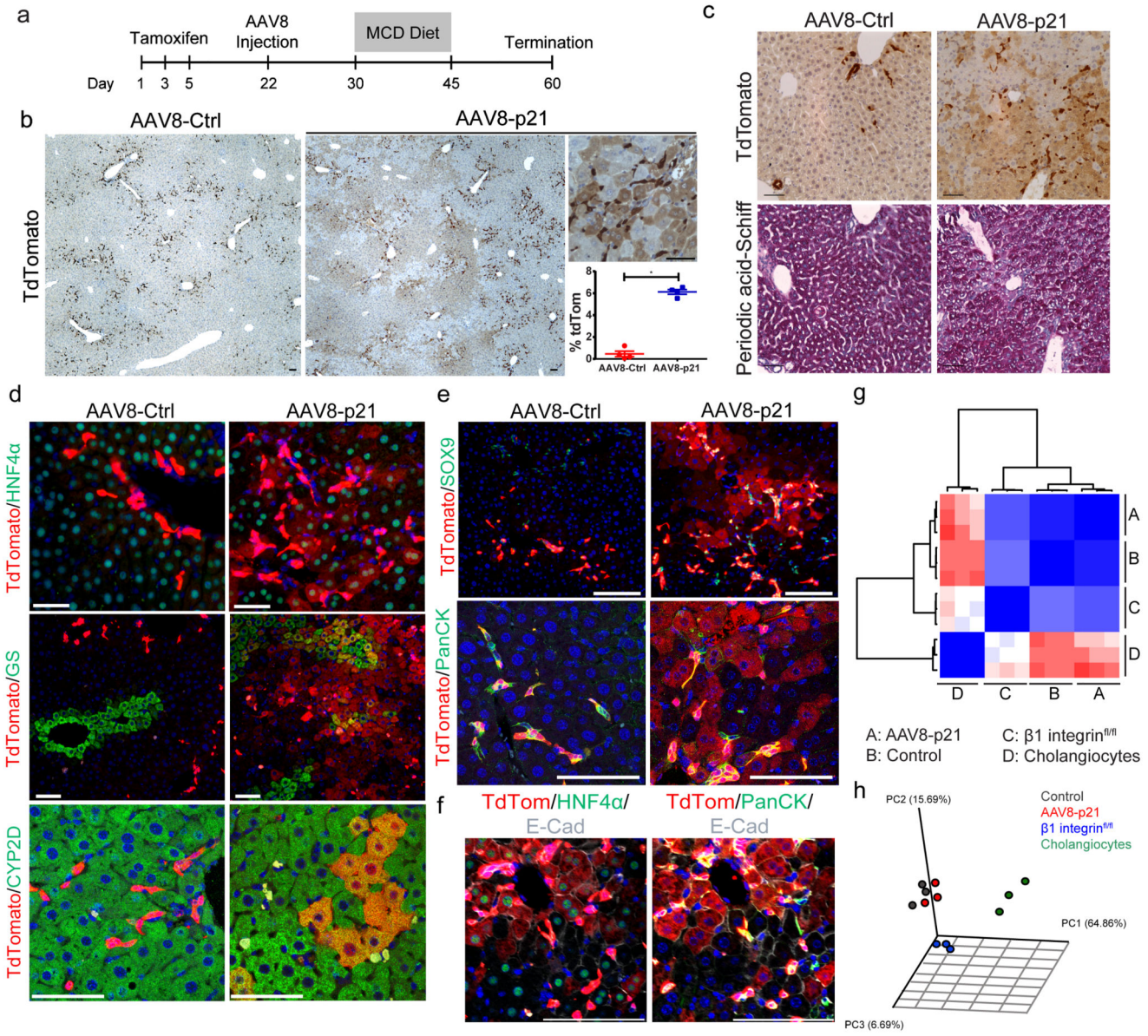

Figure 4. Emergence of ductular derived hepatocytes following chronic liver injury when hepatocyte proliferation is impaired.

a, Schematic of the MCD/recovery injury diet regime. **b,** tdTom immunohistochemistry on Krt19^{Cre}tdTomato^{LSL} livers following MCD recovery regime. High magnification images and quantification of tdTom positive cells (insets) *n*=4 mice. **c**, Immunostaining of tdTom and Periodic acid-Schiff staining on serial liver sections of AAV8 injected mice. **d,** Immunofluorescent double staining of HNF4α (green, upper panel), Glutamine Synthetase (green, middle panel), CYP2D (bottom, lower panel) and tdTom (red). **e,** DoubleImmunohistochemistry of tdTom (red), and SOX9 (green, upper panel), PanCK (green, lower panel). **f,** Confocal images of serial liver sections of AAV8 injected mice. tdTomato (red), HNF4α (green, left panel), PanCK (green, right panel), E-cadherin (grey). *n=4 mice* **g,h,** Pearson's correlation plot with hierarchical clustering and 3D Principal

Component Analysis (PCA) for total transcriptional landscapes n=3 mice. Scale Bars: 100μM. Data are representative of 1–2 independent experiments, experiments were repeated at least twice except g,h were only performed once. Data are shown as mean ± s.e.m. Mann-Whitney U-test, *P < 0.05.

Europe PMC Funders Author Manuscripts